Soft Matter

PAPER

View Article Online
View Journal | View Issue

Check for updates

Cite this: *Soft Matter*, 2023, **19**, 3614

Concentration and temperature dependent interactions and state diagram of dispersions of copolymer microgels†

José Ruiz-Franco,[abc] Rodrigo Rivas-Barbosa,[bd] Mayra A. Lara-Peña,[de] José R. Villanueva-Valencia,[d] Angel Licea-Claverie,[f] Emanuela Zaccarelli*[ab] and Marco Laurati*[e]

Received 30th January 2023,
Accepted 30th April 2023

DOI: 10.1039/d3sm00120b

rsc.li/soft-matter-journal

We investigate by means of small angle neutron scattering experiments and numerical simulations the interactions and inter-particle arrangements of concentrated dispersions of copolymer poly(*N*-isopropylacrylamide)–poly(ethylene glycol methyl ether methacrylate) (PNIPAM–PEGMA) microgels across the volume phase transition (VPT). The scattering data of moderately concentrated dispersions are accurately modeled at all temperatures by using a star polymer form factor and static structure factors calculated from the effective potential obtained from simulations. Interestingly, for temperatures below the VPT temperature (VPTT), the radius of gyration and blob size of the particles significantly decrease with increasing the effective packing fraction in the non-overlapping regime. This is attributed to the presence of charges in the system associated with the use of an ionic initiator in the synthesis. Simulations using the experimentally corroborated interaction potential are used to explore the state diagram in a wide range of effective packing fractions. Below and slightly above the VPTT, the system undergoes an arrest transition mainly driven by the soft repulsion between the particles. Only well above the VPTT the system is found to phase separate before arresting. Our results highlight the versatility and potential of copolymer PNIPAM–PEGMA microgels to explore different kinds of arrested states balancing attraction and repulsion by changing temperature and packing fraction.

1 Introduction

Microgel particles are cross-linked polymer networks of colloidal size. Their internal polymer structure can be sensitive to external stimuli, such as temperature,[1] pH,[2] or external fields,[3] by accurately tailoring its physicochemical properties. This results in colloids with variable physical and chemical properties, which offer the possibility to explore fundamental physics problems, and can be exploited in multiple applications. One of the most studied types of microgels is made of thermoresponsive poly(*N*-isopropylacrylamide) (PNIPAM), which exhibits a volume phase transition (VPT) at temperature $T_c \approx 32$ °C.[4,5] Thus, the size and stiffness of the particle can be tuned by changing the temperature.[6] In particular, for $T < T_c$, microgels are soft and display a spherical core-corona architecture, whereas for $T > T_c$, the stiffness increases and the particles undergo a collapse,[7,8] which is an echo of the underlying coil-to-globule transition of PNIPAM chains. This is driven by a change in the polymer affinity to the solvent,[9] which also results in the modification of microgel–microgel interactions at the colloidal length scale. In particular, experiments show the onset of an effective attraction in the collapsed state, signaled by aggregation and phase separation in highly concentrated suspensions.[10,11] The adaptability of PNIPAM microgels has contributed to their wide diffusion in applications such as drug delivery,[12,13] regenerative scaffolds,[14] biosensing[15] and inks for bio-interfaces design,[16] to name a few.

Furthermore, PNIPAM microgels can be programmed to have specific stimuli-response and/or additional properties through the inclusion of a second type of polymer. This inclusion can be realized in different ways: one possibility is that the second

---

[a] *CNR Institute of Complex Systems, Uos Sapienza, Piazzale Aldo Moro 2, 00185, Roma, Italy. E-mail: emanuela.zaccarelli@cnr.it*

[b] *Department of Physics, Sapienza University of Rome, Piazzale Aldo Moro 2, 00185 Roma, Italy*

[c] *Physical Chemistry and Soft Matter, Wageningen University & Research, Stippeneng 4, 6708WE Wageningen, The Netherlands*

[d] *División de Ciencias e Ingenierías, Universidad de Guanajuato, Lomas del Bosque 103, 37150 León, Mexico*

[e] *Dipartimento di Chimica and CSGI, Università di Firenze, 50019 Sesto Fiorentino, Italy. E-mail: marco.laurati@unifi.it*

[f] *Centro de Graduados e Investigación en Química del Tecnológico Nacional de México/Instituto Tecnológico de Tijuana, 22500 Tijuana, Mexico*

† Electronic supplementary information (ESI) available. See DOI: **https://doi.org/10.1039/d3sm00120b**

component is incorporated in the form of a separated shell or core, giving rise to so-called core–shell microgels. The second polymer can be non-thermoresponsive like poly(ethylene glycol) (PEG) or its methacrylated variant PEGMA, providing a more biocompatible shell for biomedical applications.[17,18] Alternatively, it can also be thermosensitive, leading to core–shell microgels exhibiting a complex swelling behavior that cannot be approximated as the sum of the transitions from each polymer.[19–21] Also classified as core–shell microgels are systems where PNIPAM acts as a shell surrounding hard particles, *i.e.*, non-thermoresponsive ones such as gold or polystyrene silica.[22,23] The resulting microgel acquires new functionalities thanks to the stimuli-responsive shell.[24] The second component can be also incorporated within the PNIPAM network, leading in this case to so-called copolymer microgels. It is possible to produce interpenetrating network (IPN) microgels, where the networks of PNIPAM and the additional polymer are chemically non-crosslinked with one another.[25,26] In this case, a microphase separation is induced by playing with the stimuli-response of each polymer type, generating a non-uniform collapse.[27,28] A different scenario occurs when polymer chains, rather than a full network, are attached within the PNIPAM network.[18,29–32] In the case of a thermoresponsive copolymer, such as poly(*N*-isopropyl-methacrylamide) (PNIPMAM) or poly-*N*,*N*-diethylacrylamide (PDEAAM), microgels present anomalous deswelling and variation of the VPT temperature.[29,30] Instead, addition of a non-thermoresponsive, hydrophilic comonomer like PEGMA leads to a shift of the VPT temperature to larger values and to a progressive reduction of the magnitude of deswelling,[17,33] that was attributed to a changed balance in hydrophobicity and hydrophilicity. In these microgels PEGMA is expected to be mainly concentrated on the exterior of the particle, due to precipitation of PNIPAM under the synthesis conditions.[17,18,31] However NMR studies in ref. 31 indicate that at least a fraction of PEGMA becomes immobilized during collapse across the VPT. Recently, through a combination of SANS measurements and monomer-resolved simulations, we confirmed that PNIPAM-*co*-PEGMA copolymer microgels exhibit a heterogeneous collapse, with the formation of two denser regions, responsible for the shift of the VPT transition to higher temperatures.[32] In the same work we also showed that the experimental particle form factor can be best described assuming that part of the PEGMA, mostly distributed on the periphery of the particle, is contained within the PNIPAM network, coherent with indications of ref. 31. Furthermore, simulations evidenced the presence in this case of an enhanced attraction above the VPT temperature, different from ionic copolymerized microgels[34] in which the effective attraction emerging from the solvophobicity of the cores can be partially shielded, preventing or retarding phase separation in highly concentrated suspensions. While previous studies allowed a thorough characterization of the single particle shape and responsiveness, essentially unexplored remains the effect of copolymerization on the inter-particle interactions at moderate and high particle concentrations and as a function of temperature. This is crucial for applications of copolymer microgels in developing electronic and photonic devices,[35,36] drug delivery[25] and cultivation of adherently growing cells.[37] In addition, the presence of PEGMA paves the way toward biomedical applications,[38–40] due to its non-cytotoxicity[41] and, thus, increased biocompatibility.

The aim of the present work is that of elucidating the interactions of copolymer microgels of PNIPAM–PEGMA. In particular, we explore a range of temperatures crossing the VPT as a function of microgel concentration. This procedure combines small-angle neutron scattering (SANS) experiments and numerical simulations. SANS measurements at different concentrations are described by using the static structure factors obtained from the effective interactions calculated through monomer-resolved simulations. We find that below and close to the VPTT, the interactions are soft and repulsive, so that a star polymer or Hertzian description well captures the structure of the resulting copolymer microgels. We also find a general reduction of the microgel size that happens before particle overlap with increasing concentration. On the other hand, above the VPTT, the size reduction is less pronounced owing to the more compact conformation. We further use the calculated effective interactions to study the static and dynamic properties of concentrated dispersions as a function of packing fraction at these different temperatures, finding the onset of dynamical arrest at relatively large packing fractions below the VPTT. Such onset is shifted to lower concentrations as T increases. At the highest studied T phase separation also occurs, thus retarding the dominant role of attraction with respect to standard PNIPAM microgels. Our results link the microgel morphology controlled by tuning the internal polymer network and its effects on the behavior of PNIPAM–PEGMA copolymer microgel dispersions.

2 Materials and methods

2.1 Experimental system

2.1.1 Microgel synthesis. Copolymer PNIPAM–PEGMA microgel particles were synthesized following a "one pot" soapless emulsion polymerization method.[33] All reagents were purchased from Sigma-Aldrich. *N*-Isopropylacrylamide (M_n = 113.16 g mol^{-1}) was purified by recrystallization in petroleum ether at 35 °C. The crosslinker ethylene glycol dimethacrylate (EGDMA, M_n = 198.22 g mol^{-1}), the initiator Ammonium Persulfate (APS) (M_n = 228.18 g mol^{-1}) and the poly(ethyleneglycol) methyl ether methacrylate (PEGMA, M_n = 950 g mol^{-1}) were used as purchased. The synthesis was carried out using a 1 L jacketed glass reactor (Syrris, model Atlas Potassium, Royston, UK) to improve temperature and stirring control. The particles were synthesized with a proportion in weight equal to 30% PEGMA and 70% PNIPAM. Initially 3.5 g of PNIPAM were dissolved in 40 ml of water and mixed with the EGDMA crosslinker (1 mol% *vs.* polymer content). The so-obtained solution was bubbled with nitrogen for 30 minutes to remove any dissolved oxygen while stirred at 350 rpm in a cold bath at 15 °C. After 20 minutes, 1.5 g of PEGMA predissolved in 10 ml of water was added to the solution and the bubbling was maintained for 10 additional minutes. The obtained mixture was added to 438 ml of preheated water

(85 °C) and stirred at 350 rpm for 30 minutes. APS (2 wt% *vs.* PNIPAM) previously dissolved in 12 ml of water was added to initiate the reaction. The polymerization was carried out for 45 minutes, after which the solution was placed in a cold bath to stop the polymerization process. The dispersion was purified *via* dialysis, using a dialysis membrane with molecular weight cut-off of 12–14 kDa and performed against distilled water for 7 days. The microgels were recovered by freeze drying. ^{1}H-NMR chracterization was performed to assess the effective incorporation of PEGMA in the synthesis, finding a final weight proportion of 66% PNIPAM and 34% PEGMA in the microgels (see ESI,† for more details, including the measured spectrum). Particle characterization performed by dynamic light scattering showed that the hydrodynamic radius $R_H \approx 166$ nm in water at low temperature T, with a polidispersity of about 25% (size distribution reported in the ESI†). The VPT occurs at $T_c \approx 36$ °C, leading to $R_H \approx 90$ nm at high T.[42] This value of T_c, also later referred as VPTT, is sensibly higher than that usually found for standard PNIPAM microgels in water ($T_c \approx 32$ °C), in agreement with previous findings,[17,31] where it was attributed to a changed balance in hydrophilicity and hydrophobicity. Recent work on PNIPAM-AAc microgels showed that changes in the VPT of PNIPAM can occur when segments smaller than 10 monomers are present, due to copolymerization.[43] The probability of such segment length is essentially negligible in our case according to the molar fractions of PNIPAM, PEGMA and crosslinker used in the synthesis. However, since the probability calculation assumes a homogeneous distribution of the components, that is not realistic in our case, small segments of PNIPAM might be present in the corona due to the higher local concentration of PEGMA.

We report in the ESI† also a SEM image of a representative PNIPAM–PEGMA collapsed particle confirming that there is no evidence of a PNIPAM(core)–PEGMA(shell) internal structure of the particles.

2.1.2 Preparation of dispersions. Dispersions with w/w concentrations c = 0.83, 2.75, 3.43 and 4.99% were prepared by redispersing the dry microgel powder in deuterated water (D_2O). After water addition, samples were heated up to 30 °C and mixed first in a vortex shaker and later with a magnetic stirrer until complete homogenization. Samples were then transferred to cuvettes for measurement. The effective volume fractions (ϕ_{eff}) of the samples at T = 20 °C were determined according to $\phi_{\mathrm{eff}} = [m_{\mathrm{coll}}/(m_{\mathrm{coll}} + m_{\mathrm{solv}})] \times [D(T = 20\ ^\circ\mathrm{C})/D_{\mathrm{min}}]^3$,[44] being T the temperature, m_{coll} and m_{solv} the mass of the colloids and solvent, respectively, and D_{min} the minimum diameter of the particles in the collapsed state at high temperature. The diameter at T = 20 °C and the minimum diameter in the collapsed state were determined by modeling the temperature dependence of the particles diameter with a logistic function.[42] Note that since even in the collapsed state at high temperatures the particles still contain a small amount of water,[45,46] the value of D_{min} estimated through the described procedure is slightly overestimated. The estimated effective volume fractions for samples at T = 20 °C are ϕ_{eff} = 0.06, 0.19, 0.24 and 0.34.

2.2 Numerical simulations

We consider copolymer PNIPAM–PEGMA microgels that were previously assembled following two steps,[32] and whose final structure was fixed using the Kremer–Grest bead-spring model.[47] Thus, all particles interact *via* a Weeks–Chandler–Andersen (WCA) potential, defined as:

$$V_{\mathrm{WCA}}(r) = \begin{cases} 4\varepsilon\left[\left(\frac{\sigma_m}{r}\right)^{12} - \left(\frac{\sigma_m}{r}\right)^{6}\right] + \varepsilon & \text{if } r \le 2^{1/6}\sigma_m \\ 0 & \text{otherwise} \end{cases} \quad (1)$$

where σ_m is the unit of length and ε controls the energy scale. Furthermore, bonded particles also interact *via* a FENE potential V_{FENE}:

$$V_{\mathrm{FENE}}(r) = -\varepsilon k_F R_0^2 \ln\left(1 - \left[\frac{r}{R_0\sigma_m}\right]^2\right) R_0\sigma_m \quad (2)$$

where k_F = 15 is the dimensionless spring constant and R_0 = 1.5 is the maximum extension of the bond. Additionally, the characteristic thermoresponsive behavior of the PNIPAM polymer is captured by adding an effective attraction among its monomers:

$$V_\alpha(r) = \begin{cases} -\varepsilon\alpha & \text{if } r \le 2^{1/6}\sigma_m \\ \frac{1}{2}\alpha\varepsilon\left[\cos\left(\delta\left(\frac{r}{\sigma_m}\right)^2 + \beta\right) - 1\right] & \text{if } 2^{1/6}\sigma_m < r \le R_0\sigma_m\,, \\ 0 & \text{otherwise} \end{cases} \quad (3)$$

with $\delta = \pi(2.25 - 2^{1/3})^{-1}$ and $\beta = 2\pi - 2.25\delta$.[48] Here, the parameter α modulates the solvophobicity of the beads, playing the role of an effective temperature in the simulations.[48,49] Indeed, we have $V_\alpha(r) = 0$ when $\alpha = 0$, reproducing good solvent conditions, whereas the VPT transition for a homopolymer microgel occurs at a critical value $\alpha_c \sim 0.65$.[50,51] On the other hand, for PEGMA monomers the effective attraction due to thermoresponsivity is ignored because it is well-known that, for this polymer, solvent quality effects become evident at a much higher temperature than for PNIPAM ones,[52] well outside the temperature range investigated in this work.

According to our previous study in ref. 32, here we focus on the case where PEGMA chains are attached within the polymer network since this conformation was found to reproduce the experimental particle morphology. For this type of copolymer microgels, the effective interaction between two microgels was evaluated by using the umbrella sampling technique at different values of α, where a series of independent configurations along a reaction coordinate are sampled by using a bias potential.[53,54] In our case, we have considered the centers of mass distance between two copolymer microgels as the reaction coordinate, with the bias potential being harmonic. Then, we evaluate the bias probability distribution $P_b(r,\Delta_i)$ of finding the macromolecules' centers of mass at distance r given the equilibrium length of the spring μ_i from our simulations. Later, the contribution from the bias potential is removed, $P_u(r,\Delta_i)$ and subsequently unbiased probability distributions are merged into $P(r)$ via a least-squares method. In this way, the potential of mean force is expressed as

$$V_{\text{eff}}(r) = -k_{\text{B}}T[P(r)] + C, \tag{4}$$

being C a constant that fixes the condition $V_{\text{eff}}(r \to \infty) = 0$.

For $\alpha = 0.0$, the effective interaction numerically calculated is well-fitted by a Hertzian model, that is usually employed for microgels,[6,55] which is expressed as

$$\beta V_{\text{H}}(r) = U(1 - r/\sigma_{\text{H}})^{5/2}\theta(1 - r/\sigma_{\text{H}}), \tag{5}$$

where U is the Hertzian strength linked to the particle elasticity and σ_{H} represents the particle diameter. The Heaviside step function θ ensures the interaction vanishes at distances $r > \sigma_{\text{H}}$. From the fit we find $U = 674.1\varepsilon$.

Instead, evidence of an effective attraction is already found for $\alpha \sim 0.5$, well below the PNIPAM VPTT, while the evaluation of the potential was possible until $\alpha = 0.7$. We could just use the calculated potential as a numerical table, but it is more practical to adopt a phenomenological analytical form. To this aim, we fit the numerical potential with the expression,

$$\begin{aligned}\beta V_{\text{eff}}(r) \;&= 4A_0\left[\left(\frac{\sigma_{\text{f}}}{r}\right)^{2A_1} - \left(\frac{\sigma_{\text{f}}}{r}\right)^{A_1}\right] \\ &\quad + A_2\left[\cos\left(A_3\left(\frac{r}{\sigma_{\text{f}}}\right)^{A_6} + A_4\right) - A_5\right] \text{ if } r \le r_{\text{cut}},\end{aligned} \tag{6}$$

where the first term acquires a generalized Lennard-Jones shape, with A_0 (in units of ε), and A_1 as fit parameters, and the second term adopts the functional form described in eqn (3), with A_2 (in units of ε), A_3, A_4 and A_5 as fit parameters. The values of the fit parameters are reported in Table S3 (ESI†), while σ_{f} represents the characteristic size of the copolymer microgel. We note that we could also describe the potential with the sum of a Hertzian plus an attractive contribution, but it appears that the former term is not able to properly capture the calculated excluded volume contribution when particles become attractive, as discussed in the SM. So, for simplicity, we stick to the phenomenological form of eqn (6), without assigning any particular meaning to the fit parameters.

Using the Hertzian potential in eqn (5) for $\alpha = 0.0$ and the attractive potentials $V_{\text{eff}}(r)$ in eqn (6) for different values of α, we then perform Langevin dynamics (LD) simulations, where the total force on the i-th particle is expressed as

$$\mathbf{F}_i = \mathbf{F}_i^{\text{C}} + \mathbf{F}_i^{\text{D}} + \mathbf{F}_i^{\text{R}}. \tag{7}$$

Here, $\mathbf{F}_i^{\text{C}} = -\nabla V_{\text{eff}}(r)$ represents the conservative force. The second term represents the drag force, defined as $\mathbf{F}_i^{\text{D}} = -\xi m_i \mathbf{v}_i$ with friction coefficient fixed to be $\xi = 10m_i/t$, m_i specifies the mass and v_i is the particle velocity. Finally, $\mathbf{F}_i^{\text{R}}$ is the random force characterized by $\langle \mathbf{F}_i^{\text{R}} \rangle = 0$ and $\langle \mathbf{F}_i^{\text{R}}(t)\mathbf{F}_i^{\text{R}}(t') \rangle = 6\xi k_{\text{b}}T\delta(t - t')$.

In all cases, we consider $N = 2000$ polydisperse particles whose diameters are described by a Schultz distribution[56] with unitary mean and standard deviation equal to PD = 25%, matching the experimental polydispersity. The packing fraction is thus defined as $\phi = \frac{\pi}{6}\langle\sigma^3\rangle\frac{N}{V}$, where V represents the volume of the simulation box. Since the temperature effects are encrypted in the effective potential interaction, we always maintain the temperature $T = \varepsilon/k_{\text{b}}$ in our simulations. All beads have unit mass, and the integration time step is $\delta t_{\text{LD}} = 0.002\sqrt{(m\langle\sigma^2\rangle)/(k_{\text{B}}T)}$. The Langevin equation was integrated using the self-adaptive OVRVO scheme, which is suitable for both equilibrium and nonequilibrium dynamics.[57,58]

2.3 Small-angle neutron scattering (SANS)

2.3.1 Measurements. SANS measurements were performed at the NG7 SANS beamline (NCNR at NIST, Gaithersburg, USA) using three different configurations: (i) 1.33 m Sample-to-Detector Distance (SDD) and incident wavelength $\lambda = 6$ Å, (ii) 4 m SDD and $\lambda = 6$ Å, and (iii) 13.17 m SDD and $\lambda = 8.4$ Å. The combination of the three configurations gives a wave vector range $0.001\ \text{Å}^{-1} < Q < 0.4\ \text{Å}^{-1}$. Measurements were performed at 20 °C, 30 °C and 40 °C.

2.3.2 Data analysis. The SANS scattered intensities measured for microgel dispersions with different packing fractions can be expressed as:[59]

$$I(Q) = \phi V(\Delta\rho)^2 P(Q)S(Q) \tag{8}$$

where ϕ is the particle volume fraction, V the particle volume, $\Delta\rho = \rho_1 - \rho_2$ the scattering length density difference between the microgels (ρ_1) and the solvent (ρ_2), $P(Q)$ the particle form factor, and $S(Q)$ the structure factor. In previous work[32] we have shown that, due to the small degree of cross-linking of the PNIPAM component (1 mol% cross-linker content), the particle form factor can be described using the star polymer form factor model of Dozier and coworkers,[60,61] that consists of two terms:

$$P(Q) = A_1 \exp\left[-\frac{1}{3}Q^2{R_{\text{g}}}^2\right] + A_2\frac{\sin\left(\mu\tan^{-1}(Q\xi)\right)}{Q\xi(1 + Q^2\xi^2)^{\mu/2}} \tag{9}$$

The first term describes the Guinier regime and provides an estimate of the particle size through the radius of gyration R_{g}. The second term is used to model the blob scattering of the star arms and allows to determine the blob size ξ. This represents the characteristic length scale at which the granular polymer structure becomes relevant. The exponent μ is defined as $\mu = 1/\nu - 1$, with ν the Flory exponent. It provides therefore information on the solvent quality conditions. The amplitudes A_1 and A_2 weight the contributions of the Guinier form factor and blob scattering terms of the model.

For $T = 40$ °C an additional blob term was included in the expression of the form factor to take into account the possible presence of structural heterogeneity of the corona induced by the presence of PEGMA inside the network that hinders the deswelling transition of PNIPAM. The expression of the form factor reads in this case:

$$P(Q) = A_1 \exp\left[-\frac{1}{3}Q^2 {R_g}^2\right] + A_2 \frac{\sin\left(\mu_1 \tan^{-1}(Q\xi_1)\right)}{Q\xi_1(1+Q^2{\xi_1}^2)^{\mu_1/2}} + A_3 \frac{\sin\left(\mu_2 \tan^{-1}(Q\xi_2)\right)}{Q\xi_2(1+Q^2{\xi_2}^2)^{\mu_2/2}} \tag{10}$$

where the last term is the second blob scattering contribution. Static structure factors $S(Q)$ at different packing fractions were calculated theoretically by solving the Ornstein–Zernike equation with the Rogers–Young closure for the effective potential obtained by umbrella sampling simulations, and for the star polymer potential proposed by Likos and coworkers,[62] defined as

$$\beta V_{\mathrm{SP}}(r) = \frac{5}{18} f^{3/2} \begin{cases} -\ln\left(\frac{r}{\sigma_{\mathrm{eff}}^{\mathrm{SP}}}\right) + \frac{1}{1+\sqrt{f}/2} & \text{for } r \le \sigma_{\mathrm{eff}}^{\mathrm{SP}} \\ \frac{\sigma_{\mathrm{eff}}^{\mathrm{SP}}/r}{1+\sqrt{f}/2}\left[\exp -\frac{\sqrt{f}\left(r-\sigma_{\mathrm{eff}}^{\mathrm{SP}}\right)}{2\sigma_{\mathrm{eff}}^{\mathrm{SP}}}\right] & \text{for } r \ge \sigma_{\mathrm{eff}}^{\mathrm{SP}} \end{cases}, \tag{11}$$

where f is the number of star arms, called functionality, and $\sigma_{\mathrm{eff}}^{\mathrm{SP}}$ is the characteristic size of a star polymer. For each sample a set of structure factors was calculated for different values of the effective packing fraction. The numerically calculated structure factors $S(Q)$ were interpolated on the experimental Q values and multiplied by the model form factor to fit the data in SasView.[63] The fitted effective packing fraction, ϕ, that takes into account the shrinking of the microgels at higher T and is thus a true packing fraction similar to the simulation one, was obtained from that of the structure factor that provides the best fit of the SANS data. In particular, for the star potential we used $f = 500$, according to previous work.[32]

For the potential calculated for $\alpha = 0.7$, the copolymer microgel collapses (see Fig. 1(a)), and we find the occurrence of phase separation also at very low packing fractions. This is also confirmed by the calculation of the second virial coefficient normalized to the hard sphere value, B_2^*, also reported in Table S3 (ESI†). To compare to experimental data, which do not show phase separation in the SANS investigated range, we adopt an interpolation of the effective potential in the range $\alpha \in [0.5, 0.7]$. In order to choose the right value of α we use the following additional information from experiments: (i) at 40 °C the system presents phase separation at a packing fraction $\phi_{\mathrm{eff}} \sim 1.6$, amounting to $\phi \gtrsim 0.18$, as indicated by the strong increase of turbidity and by additional velocimetry measurements, which show the occurrence of total slip in the sample, a typical response of attractive samples;[64] (ii) at 30 °C full phase separation is never observed, although at large packing fractions the system displays characteristic features of gelation. Taking into account these facts, we consider effective potentials at a value of α for which these features are approximately reproduced and, at the same time, that are able to fit the experimental SANS data. The interaction potentials that fulfill these requirements correspond to roughly $\alpha = 0.5$ for 30 °C and $\alpha = 0.58$ for 40 °C and are shown in Fig. 1(b).

3 Results

3.1 Effects of concentration below the VPTT

The experimental SANS scattering intensities measured at T = 20 °C for increasing ϕ_{eff} (Fig. 2) show the progressive appearance of a peak in the region for $Q < 10^{-2}$ Å^{-1}, that indicates the increasing contribution of interactions through the structure factor $S(Q)$. The peak moves to larger Q values with increasing ϕ_{eff} as a consequence of the reduced inter-particle average distance. However, we notice that the whole intensity

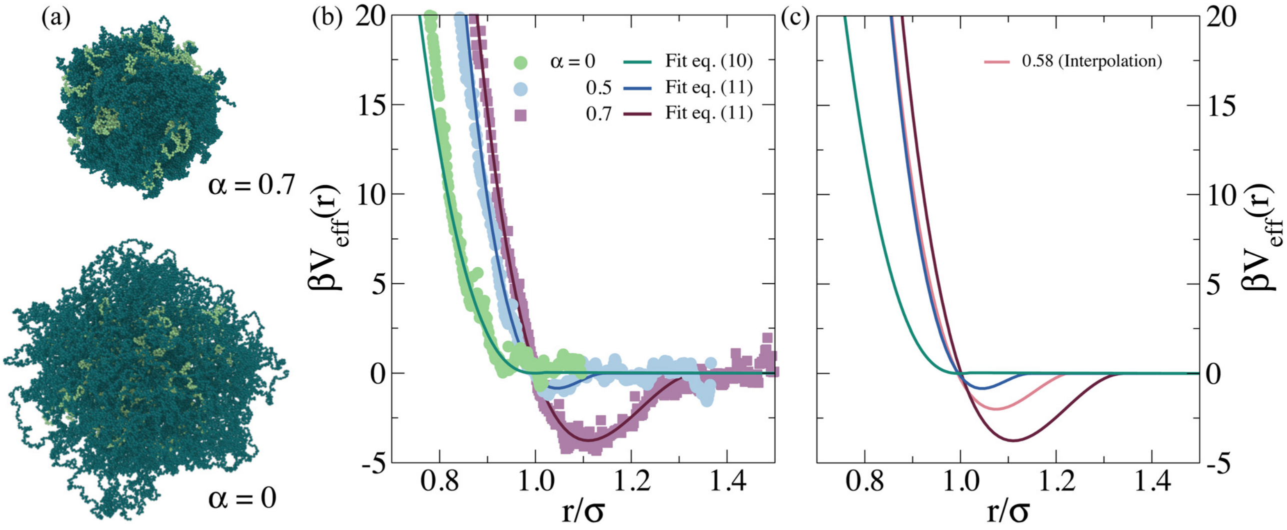

Fig. 1 (a) Snapshots from monomer-resolved simulations for copolymer microgels at $\alpha = 0$ and $\alpha = 0.7$. Here, light and dark green colors correspond to the PEGMA and PNIPAM monomers, respectively. (b) Effective potential $\beta V_{\mathrm{eff}}(r)$ obtained by umbrella sampling (symbols) and their respective fits (lines) as a function of the effective temperature α. (c) Only $\beta V_{\mathrm{eff}}(r)$ extracted from the fits are shown, with the additional curve for 0.58 obtained by interpolation.

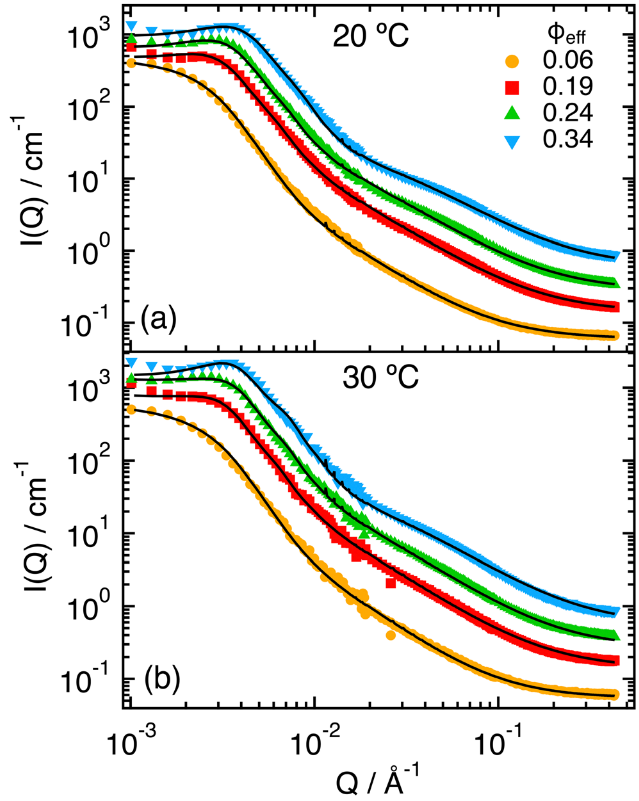

Fig. 2 SANS scattering intensities $I(Q)$ for ϕ_{eff} = 0.06, 0.19, 0.24, 0.34, as indicated, and T = 20 °C (a) and 30 °C (b). Lines represent fits in which the structure factor $S(Q)$ has been calculated by modeling the interactions through the effective potential obtained from simulations for α = 0 (a), or α = 0.5 (b). Data and fits for ϕ_{eff} = 0.19, 0.24 and 0.34 were vertically shifted by factors 2, 4, 8, respectively, for better visualization.

curve progressively shifts towards larger Q values, which indicates that the particle size also reduces with increasing ϕ_{eff}. One can also note the growth of a shoulder at around $Q \approx 7 \times 10^{-2}$ Å^{-1} with increasing packing fraction. This is reminiscent of what was observed for the form factor when increasing T across the VPT,[32] where it was associated to the progressive shrinking and compaction of the particles and the formation of a non-uniform density profile due to the presence of the PEGMA within the PNIPAM network. For samples with $\phi_{\text{eff}} \geq 0.19$ some extra scattering in the region of low Q-values before the structure factor peak might be the result of inhomogeneities and partial aggregation. This extra scattering was not considered in the modeling presented in what follows. Similar behavior was observed for the measurements at T = 30 °C, that are reported in Fig. 2b.

3.1.1 Modeling: effective potential from simulations and star polymer potential.

The results of modeling the scattering intensities at T = 20 °C using eqn (8), in which the static structure factor was calculated for the effective potential determined for simulations with α = 0, are reported in Fig. 2a. For all experimental intensities a satisfactory description of the data is obtained, except for small discrepancies in the region of the lowest Q-values where, as already commented, additional effects which are not included in the model might be present. Comparable results are obtained for T = 30 °C with α = 0.5, shown in Fig. 2b. A satisfactory description of the data is also obtained using structure factors calculated using the star polymer potential (see ESI†). The parameters obtained from the fits at T = 20 °C and 30 °C are reported in Table S1 of the ESI.†

3.1.2 Dependence of the fit parameters on concentration.

We now discuss the concentration dependence of the parameters obtained from the fits reported in the previous section. Fig. 3 shows the dependence of the fit parameters R_g, ξ_1, μ_1 and ϕ on the effective packing fraction ϕ_{eff}, estimated as reported in Section "Preparation of dispersions". For both potentials and explored temperatures the value of R_g is found to decrease considerably with increasing ϕ_{eff}, reducing to about half of its value when going from ϕ_{eff} = 0.06 ($R_g \approx$ 800 Å) to ϕ_{eff} = 0.34 ($R_g \approx$ 400 Å) (Fig. 3a). The reduction can be described by an approximately linear dependence on ϕ_{eff}. It is interesting to observe that the investigated samples present effective packing fractions which are still quite moderate, being ϕ_{eff} = 0.34 the maximum investigated packing fraction. Therefore, particle deswelling and deformation due to particle contacts should not play a significant role on the observed shrinking. However, the particles were synthesized using the ionic initiator ammonium persulfate, that induces the presence of charges through SO_3^- groups, which concentrate mostly at the ends of the PNIPAM chains, *i.e.* on the surface of the particles. Most of the associated NH_4^+ counterions are bound to the gel network forming a cloud that extends outside the gel. In addition, a small fraction is freely moving outside and mainly contributes to osmotic pressure at sufficiently small microgel concentrations. Previous works[65,66] have shown that at sufficiently large packing fractions the clouds of the microgels overlap and percolate, and the number of free counterions increases, providing an additional contribution to the osmotic pressure that increases outside the particles. This generates an unbalance in the osmotic pressure inside and outside the particles, that can lead to deswelling when it becomes comparable or larger than the bulk modulus of the particles.[65,66] We can therefore speculate that the observed reduction in R_g is induced by charge effects. Compared to the studies in ref. 65 and 66, significant deswelling is observed at smaller ϕ_{eff} in our case. This might be due to the fact that the copolymer particles studied in this work present a significantly different internal structure compared to microgels obtained using bis-acrylamide (BIS) as crosslinker. Indeed, EGDMA is expected to react significantly faster than BIS with PNIPAM.[67,68] This leads to particles with small cores that contain most of the crosslinker, and extended, poorly crosslinked coronas. The internal structure of the particles should be then similar to that of a star polymer, as supported by the fact that the particle form factor measured by SANS is better described by a star-polymer model compared to the fuzzy sphere model conventionally used for microgels. Due to the presence of charges on the external part of the corona, our particles could thus resemble star polyelectrolytes[69] or DNA coated star-like colloids.[70,71] The star-like conformation with the extended and poorly cross-linked corona, together with the

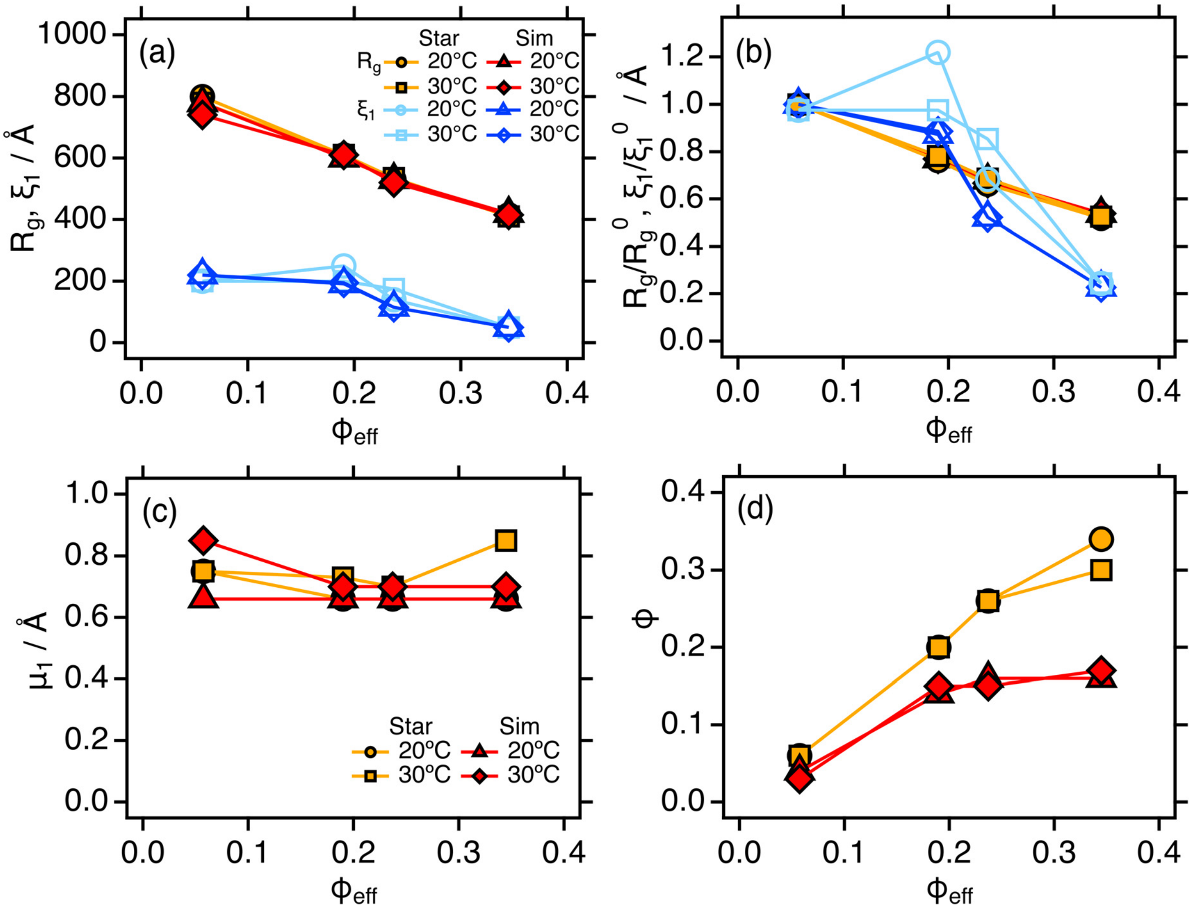

Fig. 3 Parameters obtained by fitting the SANS scattering intensities $I(Q)$ using eqn (8), with the form factor $P(Q)$ corresponding to the Dozier model of eqn (9) and the structure factor $S(Q)$ calculated by modeling the interactions through the potential obtained from simulations (with α = 0.0 for 20 °C and α = 0.5 for 30 °C) or from the star polymer potential (with f = 500), as a function of ϕ_{eff}: (a) radius of gyration R_g and blob size ξ_1, (b) Same parameters normalized by their values at the smallest value of ϕ_{eff}, R_g^0 and ξ_1^0. (c) Exponent μ_1 and (d) packing fraction used for the calculation of $S(Q)$, ϕ.

lower degree of crosslinking (1% crosslinker *vs.* 2% crosslinker concentration), is expected to be reflected in a larger softness than microgels investigated in the previous studies. Using the approach proposed by Scotti and coworkers,[65] we estimated the osmotic unbalance due to free ions for a change in packing fraction from 0.06 to 0.34, the extreme values of ϕ_{eff} measured (see ESI†). By equating this value to the variation of elastic energy corresponding to a deswelling ratio $\Delta R/R \approx 0.5$, as observed in the experiments, we obtain a value of the bulk modulus of the microgels $K \approx 1.4$ kPa, that is comparable to that of ultra-low-crosslinked microgels[72] and thus reasonable also for our system. Finally, we note that a star-like internal structure, in which the corona is always significantly larger than the core, could imply a comparable softness of particles with different sizes (according to the large size distribution). This seems to be reflected in the small variations of polydispersity obtained from the fits (see ESI†).

Concerning the blob size, one observes (Fig. 3a) that it remains almost constant up to ϕ_{eff} = 0.19 ($\xi_1 \approx 200$ Å) and then reduces down to about one fourth for ϕ_{eff} = 0.34 ($\xi_1 \approx 50$ Å). Moreover, the relative shrinkage of the blob, ξ_1/ξ_1^0, at high ϕ_{eff} values becomes larger than that of the core, R_g/R_g^0 (Fig. 3b), where R_g^0 and ξ_1^0 are the values of R_g and ξ obtained at the smallest measured ϕ_{eff}. According to the Daoud and Cotton model of a star polymer,[73] the blob size and radius of gyration should be linked through the expression $\xi = 2R_g/\sqrt{f}$, being f the number of arms of the star. The different dependence on ϕ_{eff} observed for R_g and ξ thus suggests that the effective value of f for the microgels changes with changing packing fraction, which reflects a change in the conformation of the polymer chains for the different values of ϕ_{eff}. In particular, the stronger reduction of ξ at large ϕ_{eff} would correspond to an increase in f, that is consistent with a compaction of the microgel due to collapse. Note also that the relative variation of ξ and R_g appears similar to that of the corona and core observed for T-induced deswelling of PNIPAM microgels with the same kind of ionic initiator.[74]

The coefficient μ_1 remains approximately constant as a function of ϕ_{eff} for both temperatures. At T = 20 °C we found $\mu \approx 0.66$, which corresponds to good solvent conditions ($\nu = 3/5$). It increases slightly for T = 30 °C, as expected from the closer vicinity of this temperature to the LCST. Finally, the packing fraction used to calculate the structure factors used to model the data, ϕ, shows a different trend for the two interaction potentials

(Fig. 3d). For the star polymer potential it is approximately equal to ϕ_{eff}, except for the most concentrated sample, where it is slightly smaller. Instead, for the calculated effective potential in Fig. 1, ϕ is initially slightly smaller but comparable to ϕ_{eff}, while it remains almost constant around $\phi = 0.16$ for $\phi_{\mathrm{eff}} \gtrsim 0.2$. This trend might be reflecting the progressive reduction in particle size that we associated with charge effects, that competes with the increase in particle number density.

3.2 Effects of concentration above the VPTT

The SANS intensities measured at $T = 40$ °C (Fig. 4) for increasing ϕ_{eff} show, as for the lower temperatures, changes in the region $Q < 10^{-2}$ Å^{-1} associated with the effects of the structure factor $S(Q)$. However, in this case the variation is much more moderate and does not result in a clear peak in $I(Q)$. This can be attributed to the particle deswelling that occurs above the VPTT, and the consequent reduction of the effective volume fraction of the system. In addition, one observes that the Guinier regime of the curves shifts to larger Q values with increasing ϕ_{eff}, indicating a further reduction of the particle size with increasing packing fraction. Finally, one can notice the presence of a pronounced shoulder around $Q \approx 10^{-2}$ Å^{-1}, which has been associated in previous work to the non-homogeneous density profile of the particles at high T, that is induced by the presence of the unresponsive PEGMA in the interior of the PNIPAM network.[32] Note that the shoulder becomes increasingly pronounced with increasing ϕ_{eff}, and that an additional small inflection seems to develop around $Q \approx 10^{-1}$ Å^{-1} for the samples with larger ϕ_{eff}.

3.2.1 Modeling: effective potential from simulations. For $T = 40$ °C the SANS intensities were modeled using the form factor of eqn (10), that contains an additional blob term used to model the density heterogeneities discussed previously, and structure factors $S(Q)$ calculated for the potential obtained from simulations with $\alpha = 0.58$. The results of the fits were satisfactory for all values of ϕ_{eff} (Fig. 4). Only in the region around the first inflection point after the Guinier regime, for $Q \approx 10^{-2}$ Å^{-1}, the model seems to predict a slightly smoother decay than for the experimental data. The parameters obtained from the fits are reported in Table S1 of the ESI.† The parameter trends are discussed in the next section. For the data at 40 °C we did not test the alternative use of the star polymer potential to calculate the structure factor, since this does not include an attractive component.

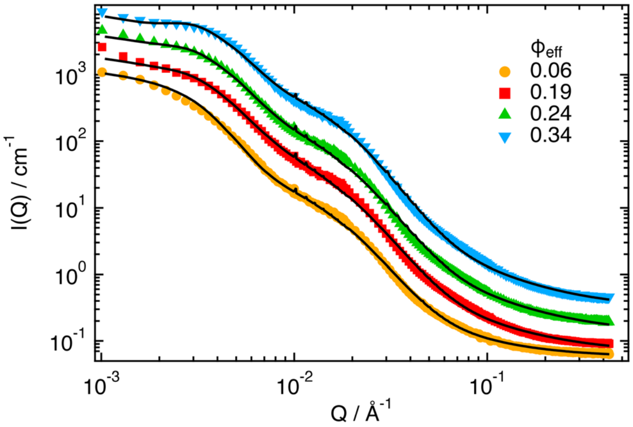

Fig. 4 SANS scattering intensities $I(Q)$ for $\phi_{\mathrm{eff}} = 0.06, 0.19, 0.24, 0.34$, as indicated, and $T = 40$ °C. Lines represent fits in which the structure factor $S(Q)$ has been calculated by modeling the interactions through the effective potential obtained from simulations for $\alpha = 0.58$. Data and fits for $\phi_{\mathrm{eff}} = 0.24$ and 0.34 were vertically shifted by factors 2 and 4, respectively, for better visualization.

3.2.2 Dependence of the fit parameters on concentration. Changes in the particle size as a function of ϕ_{eff} are summarized in the parameters R_g, ξ_1 and ξ_2 reported in Fig. 5a. One can clearly see that while R_g and ξ_1 still decrease with increasing packing fraction, the variations are much less pronounced than below the VPTT. This is even more clearly seen in Fig. 5b, that reports the relative variations with respect to the values obtained for the smallest ϕ_{eff}. There one sees also that, as for the lower temperatures, ξ_1 starts to decrease for $\phi_{\mathrm{eff}} > 0.2$. However, this time no crossing between R_g/R_g^0 and ξ_1/ξ_1^0 is observed. It is interesting also to note that the parameter ξ_2 instead starts to increase for $\phi_{\mathrm{eff}} > 0.2$.

The values obtained for the exponents μ_1 and μ_2 (Fig. 5c) shed some light on the different nature of the two blob terms. Indeed μ_1, which was already associated to the blob scattering of PNIPAM below the VPTT, attains now a value of about 2, which is consistent with the poor nature of the water solvent at $T = 40$ °C ($\nu = 1/3$). It is also approximately constant for all samples. Instead μ_2, which is also constant for all values of ϕ_{eff}, presents a value of 0.66, which indicates good solvent conditions ($\nu = 3/5$). This suggests that the second blob term can be associated with the PEGMA chains. Results in Fig. 5b thus indicate that the size of PEGMA blobs tends to slightly increase with packing faction, possibly as an effect of a larger available volume when the PNIPAM chains collapse.

Finally, the values of the fitting packing fraction ϕ are quite small and slightly increase with increasing ϕ_{eff}. This is consistent with the deswelling transition, that leads to a consistent reduction of the packing fraction associated with the reduction of the particle size. The fact that the value increases monotonically is different from what observed at smaller temperatures. This is however in agreement with the fact that the size reduction induced by the increase of ϕ_{eff} is now much less pronounced, and therefore does not dominate over the increase in particle number density as for the lower temperatures. Finally, we note that the highest measured ϕ is still below the value at which we find indications of phase separation ($\approx$0.18), consisting in a strong increase of turbidity and the onset of total wall slip in velocimetry measurements, as already mentioned in section ''Data analysis'' (data not shown).

3.3 Arrested states in copolymer microgels

The satisfactory comparison between measured and calculated scattering intensities has validated the effective interactions that we have estimated from simulations over the investigated range of packing fractions. Now, we use simulations to extend such range and to study theoretically the behavior of the dispersions at higher packing fractions until an arrested state

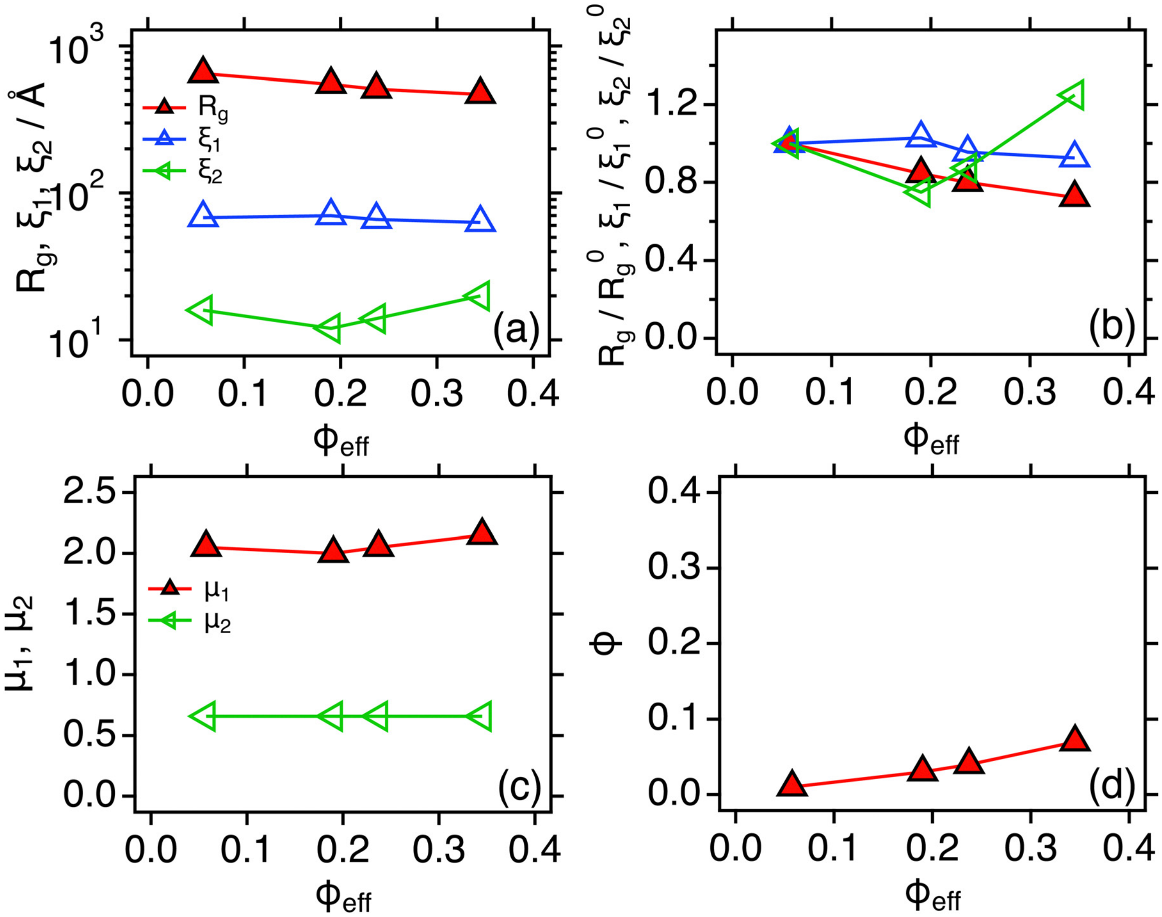

Fig. 5 Parameters obtained by fitting the SANS scattering intensities $I(Q)$ using eqn (8), with the form factor $P(Q)$ corresponding to the Dozier model of eqn (9) and the structure factor $S(Q)$ calculated by modeling the interactions through the potential obtained from simulations for $\alpha = 0.58$, as a function of ϕ_{eff} (a) radius of gyration R_g and blob sizes ξ_1 and ξ_2, (b) Same parameters normalized by their values at the smallest value of ϕ_{eff}, R_g^0, ξ_1^0 and ξ_2^0, (c) Exponents μ_1 and μ_2, (d) Packing fraction used for the calculation of $S(Q)$, ϕ.

is formed or the onset of phase separation is detected. To this aim, we perform LD simulations of polydisperse particles with PD = 25%. We consider the three different effective interactions, corresponding to the three temperatures studied in experiments ($\alpha = 0.0, 0.50, 0.58$). At $T = 20$ °C, the interactions are fully compatible with a repulsive Hertzian model, described in eqn (5). For the other two temperatures, an additional attraction arises in the effective potential, and we use the phenomenological expression given in eqn (6), with the parameters provided in Table S3 (ESI†). In the simulations, we monitor both static and dynamic properties with varying ϕ until the system is not able to equilibrate any longer due to an intervening arrest or phase separation.

First, we calculate the static structure factors $S(Q)$ of the polydisperse system, defined as

$$S(Q) = \frac{1}{N\overline{b^2(Q)}}\left\langle \sum_{ij} b_i(Q) b_j(Q) \exp\left[-i\mathbf{Q}\cdot(\mathbf{r}_i - \mathbf{r}_j)\right]\right\rangle, \quad (12)$$

with $\mathbf{r}_i$ indicating the position and $b_i(Q)$ the scattering amplitude of the i-th particle, the latter being different for each particle size, following ref. 75, $\overline{b^2(Q)}$ being averaged over all particles and $\langle\cdots\rangle$ the average over different configurations. From Fig. 6a, we see that at low temperatures a non-monotonic behavior of the main peak of $S(Q)$ occurs for $\phi \gtrsim 0.50$. This loss of local order is typical of Hertzian systems, where a reentrant behavior of static correlations has been previously reported.[76,77] However, interestingly, the addition of a large polydispersity in the present system introduces a novel feature in the behavior of $S(Q)$ with respect to monodisperse Hertzian, namely that with the further increase of ϕ the first peak eventually goes below 1. We thus wonder whether we are seeing an unphysical behavior due to the pure Hertzian modeling. Indeed, it is well-known that microgels have a complex inner structure, with a more compact core, that has been for example modeled as a multi-Hertzian to take this into account.[78] We thus repeat simulations for representative state points, where we consider the addition of a steeper repulsion, modeling the inner core, at shorter distances, as discussed in more detail in the ESI.† The size of the inner core is taken from the experimental R_g. We find that the effects of the core are not observed in the investigated range of ϕ and its presence

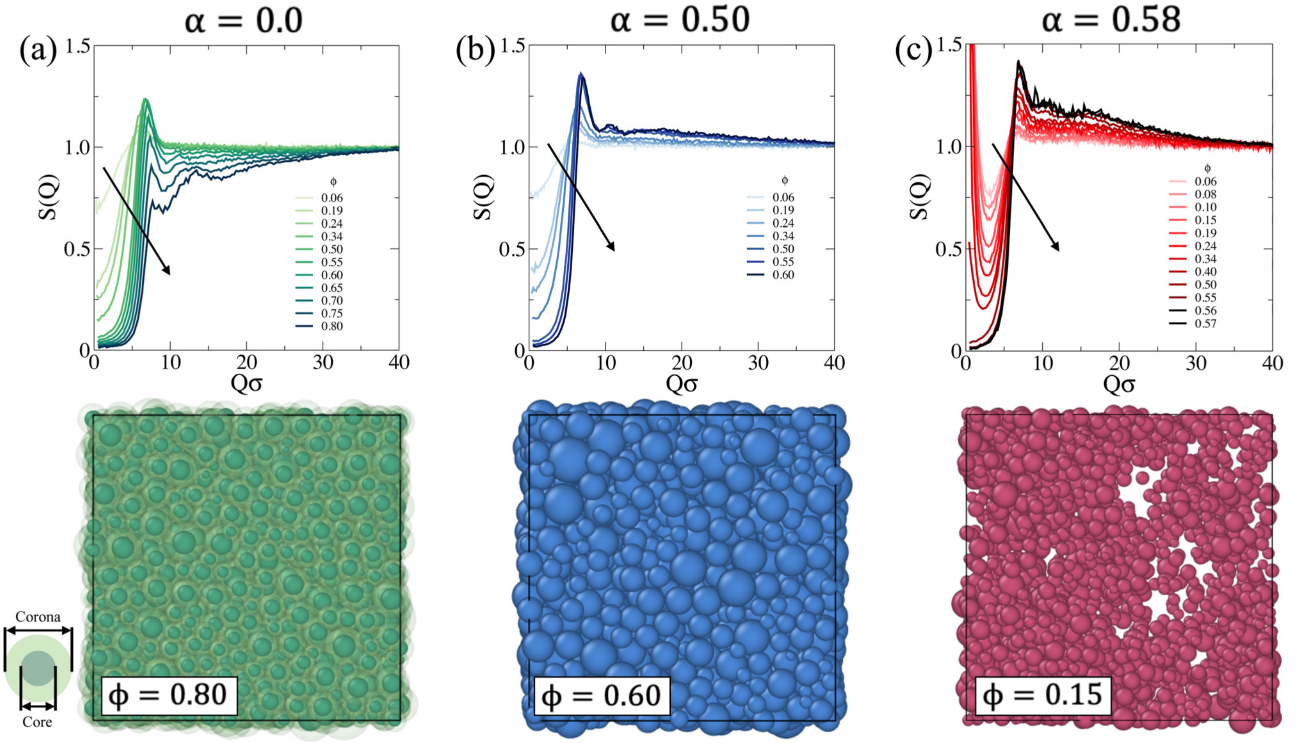

Fig. 6 Static structure factor $S(Q)$ as a function of the packing fraction ϕ (top), and corresponding snapshots (bottom) for (a) $\alpha = 0.0$, (b) $\alpha = 0.50$ and (c) $\alpha = 0.58$. The core region reported for $\alpha = 0.0$ is the one estimated from the experimental R_g. The arrow highlights the increase in ϕ.

becomes evident only at much larger packing fractions, where dynamical arrest has already taken place (as shown below). Thus, the anomalous feature of $S(Q)$ having the main peak below 1 is the result of the combination of the Hertzian model and the large polydispersity of the system, as also discussed in the ESI.† It is important to note that similar behaviors of $S(Q)$ at high concentrations have been previously reported for polydisperse eye-lens proteins[79] and also, for anisotropic antibodies.[80] It remains to be investigated in the present systems whether such features hold at high ϕ, where steeper excluded volume effects may enter into play and prevent the softening related to the Hertzian modeling. This should be addressed in future works by performing measurements of the system at higher ϕ or by trying to perform simulations of monomer-resolved microgels, rather than of a coarse-grained model.

We now focus at intermediate temperatures ($\alpha = 0.5$), where the addition of a moderate attraction has significant effects on the structure, as shown in Fig. 6b. In particular, we can equilibrate the system up to $\phi \sim 0.62$, above which the dynamics becomes too slow (as discussed in the following) and, contrary to the $\alpha = 0.0$ case, we do not observe a reentrance in the first peak of $S(Q)$. Rather, the peak monotonically increases as in standard fluids. This indicates that the attraction is compensating the Hertzian tendency to shrink and thus induce a reentrant behavior. In addition, at high Q, we observe a structure factor that is overall staying above 1, again contrary to the case of $\alpha = 0.0$ where it is largely below this. However, we can exclude any sign of heterogeneity in the samples, as there is no upturn of $S(Q)$ visible at low Q, as also evident from the snapshots, shown in Fig. 6b. This is also confirmed by the fact that the large-Q behavior of $S(Q)$ tends to 1 in all cases. Completely different is the situation at $\alpha = 0.58$, shown in Fig. 6c, where we clearly detect phase separation, that is evident in the $\phi = 0.15$ snapshot and also from the increase in $S(Q \to 0)$. We did not follow the phase separation in detail and do not aim to trace a rigorous boundary for it from simulations, but just to qualitatively establish the behavior of the system for this value of α in comparison to experiments, where also phase separation at effective packing fractions above those studied by SANS was detected. Interestingly, we again find homogeneous systems for $\phi \gtrsim 0.50$, as shown from the behavior of $S(Q)$ at low wavevectors. In this case, we can equilibrate the system up to $\phi \sim 0.57$.

On the basis of these results, we then monitor the dynamics and approach dynamical arrest of the microgels outside the phase separation region. First, we calculate the mean squared displacement (MSD) $\langle \Delta r^2(t) \rangle$, expressed as

$$\langle \Delta r^2(t) \rangle = \left\langle \frac{1}{N} \sum_{i=1}^{N} [\mathbf{r}_i(t) - \mathbf{r}_i(0)]^2 \right\rangle. \tag{13}$$

MSD results are shown in Fig. 7a. At $T = 20$ °C, the system begins to display signs of arrest at $\phi \sim 0.65$, where a plateau in the MSD develops, signaling the onset of caging. This plateau becomes longer and longer until $\phi = 0.80$, that is the highest value of ϕ that we are able to equilibrate within our simulation time.

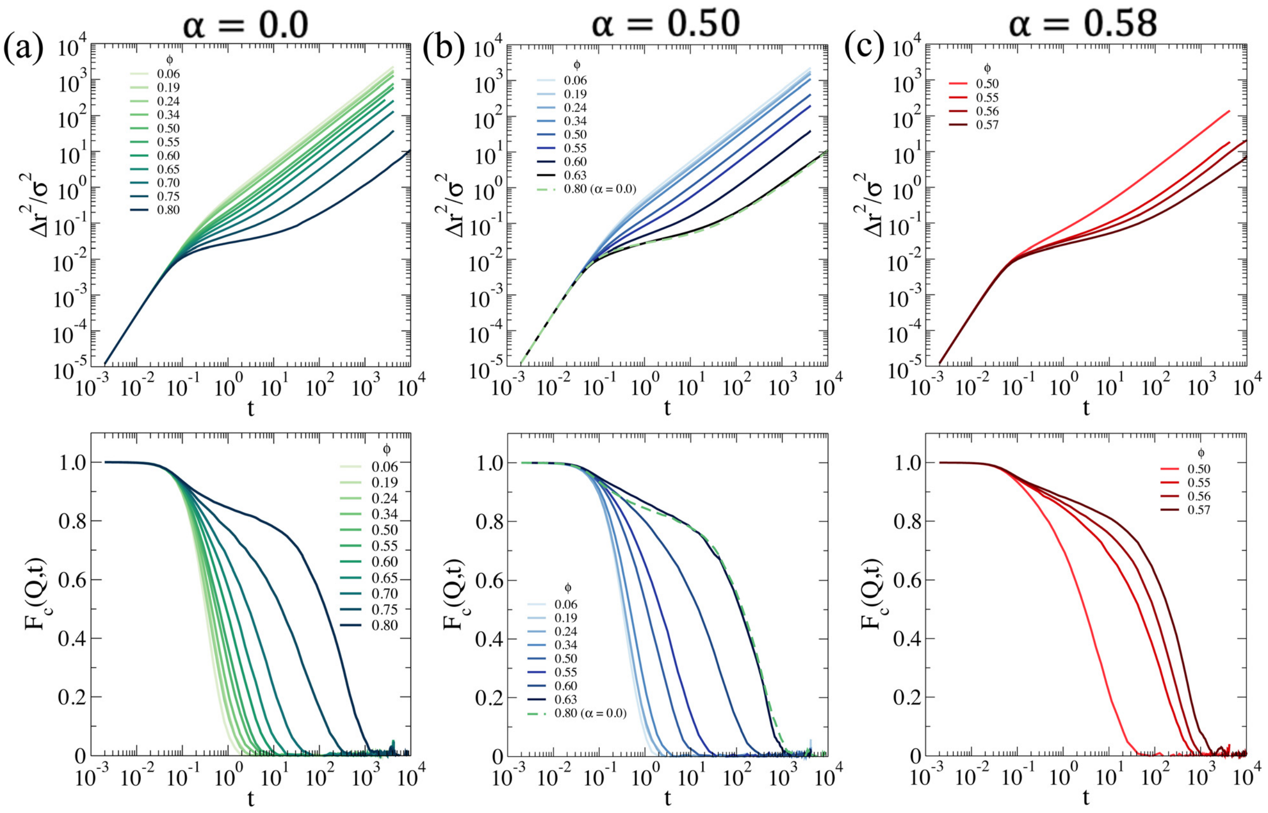

Fig. 7 Dynamic properties for a system interacting with the effective potential corresponding to (a) α = 0.0 (b) α = 0.50 and (c) α = 0.58: (top) mean squared displacement $\Delta r^2(t)$; (bottom) collective intermediate scattering function $F_c(Q,t)$ calculated at the associated Q value where $S(Q)$ is maximum.

On the other hand, the arrested state at T = 30 °C occurs at much smaller packing fractions. However, it is interesting to note that if we superimpose the MSD at ϕ = 0.63 for T = 30 °C and ϕ = 0.80 for T = 20 °C, which share a similar value of the self-diffusion coefficient, the two behaviors are quite similar to each other. Hence, despite the clear differences observed in the behavior of $S(Q)$, the approach to dynamical arrest seems to be similar for these two cases. Hence, the presence of attraction at the higher temperature favours the formation of bonds between the microgels and, thus, induces an anticipated arrest at a lower ϕ, but once this is obtained, the exploration of the cage, the average localization and the time to diffusion are very similar between the two states (with the exception of minor changes in the exploration of the plateau, not visible due to the log–log scale). This is because attraction is of very low-strength (with the minimum depth of the potential $\sim -1k_BT$, see Fig. 1) and, therefore, both arrested states are eventually dominated by the short-distance Hertzian repulsion. We also calculate MSDs for the non-phase-separating states at α = 0.58, which suggest that at the end of phase separation the system is still ergodic, becoming arrested for $\phi \gtrsim 0.55$.

Next, we compute the collective intermediate scattering function $F_c(Q,t)$, defined as

$$F_c(Q,t) = \left\langle \frac{1}{N}\sum_{i,j}^{N} \exp\left[i\mathbf{Q}\cdot\left(\mathbf{r}_i(t+t') - \mathbf{r}_j(t')\right)\right] \right\rangle, \qquad (14)$$

focusing on the wavevector corresponding to the main peak of the static structure factor for both temperatures. The bottom panels of Fig. 7 report the behavior of $F_c(Q,t)$, normalized by its zero-time value, *i.e.* $F_c(Q,0) = S(Q)$. Again we observe the emergence of the characteristic two-step decay, signaling dynamical arrest. The first step, occurring at short times, is a consequence of the interactions of the particles with their neighbors that form cages. On the other hand, the second step, taking place at longer times, indicates the final α-relaxation of the system, so that ergodicity is restored. For all studied values of α, the system displays a similar dynamical behavior. Repeating the direct comparison between the curves for α = 0.0 and α = 0.5 at the highest studied ϕ's, we again find that the final relaxation is very similar between the two, but some differences are present in the exploration of the cage, probably also due to the underlying different structure. In particular, we notice that the more attractive state displays a slower approach to the plateau, characterized by a slightly larger value of $F_c(Q)$ at intermediate times. This is consistent with expectations that the presence of bonds between the particles slightly reinforces the local cages where particles are initially trapped. Once particles are able to get out of the nearest-neighbour cage, the two dynamics become almost identical, again because dominated by the Hertzian repulsion. For α = 0.58, we find a similar behavior, characterized by a further increase in $F_c(Q)$ in the plateau region, although occurring at a smaller ϕ, which

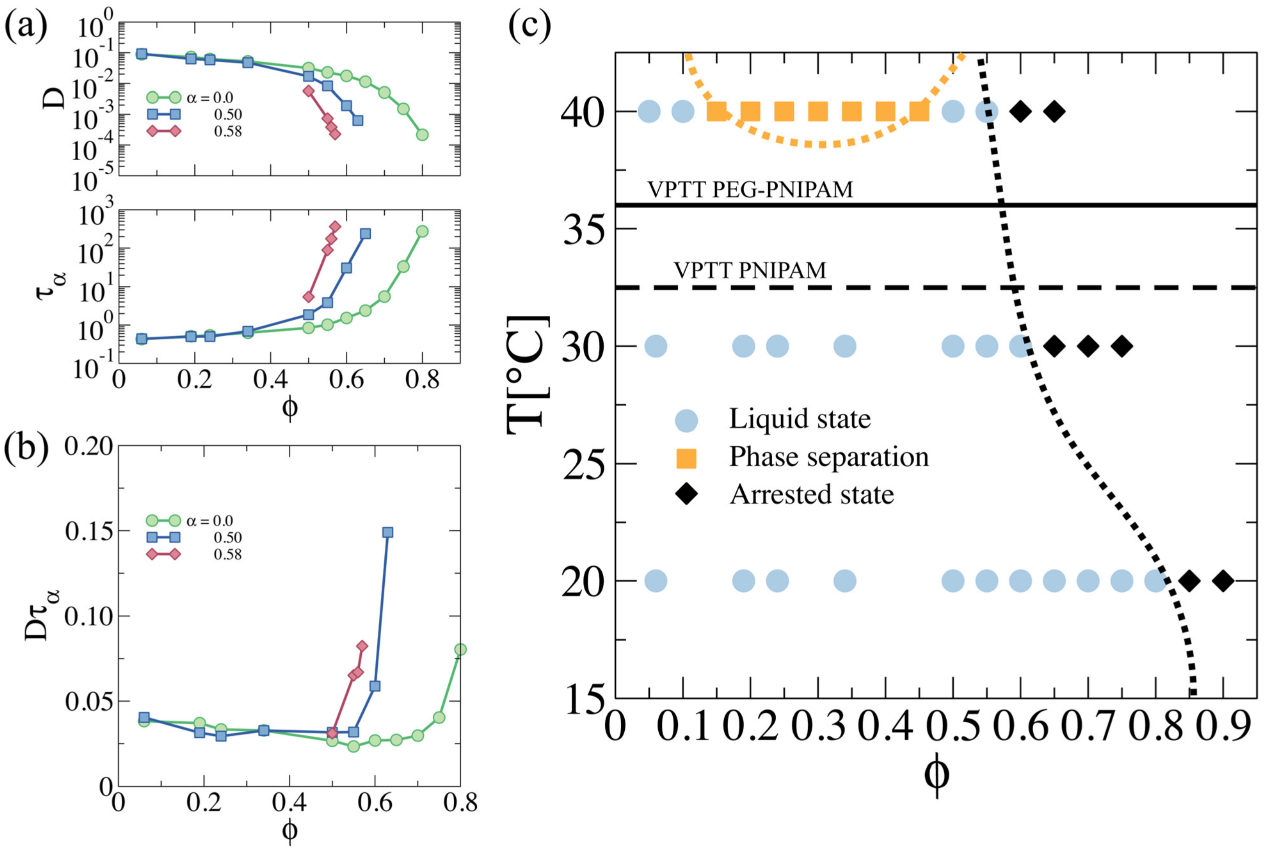

Fig. 8 (a) Self-diffusion coefficient D and collective relaxation time τ_α and (b) $D\tau_\alpha$ product as a function of ϕ at the three studied temperatures; (c) tentative phase diagram. Horizontal dashed and full lines correspond to the VPTT for PNIPAM and PNIPAM–PEGMA copolymer microgels, respectively. Likewise, the black dotted line is a guide to the eye of the onset of the arrested state, whereas the orange dotted line indicates the approximate phase separation boundary.

confirms the increasing role of the attraction in driving the dynamical arrest.

Finally, we try to sketch a phase diagram using the information inferred from the static properties at a single microgel and dynamics features explored by numerical simulations of samples with copolymer microgel. To determine the glass region, we first extract the long-time self-diffusion coefficient defined as

$$D = \lim_{t\to\infty} \frac{\langle \Delta r^2 \rangle}{6t}, \tag{15}$$

and we also calculate the α-relaxation time, τ_α, as $F_c(Q,\tau_\alpha) = 1/e$. Fig. 8(a) reports the behavior of D and τ_α as a function of ϕ for the three studied temperatures. We find that the dependence of the data on ϕ is not satisfactorily fit by a power-law behavior, for which we would probably need more state points close to arrest. However, when we plot the product $D\tau_\alpha$, shown in Fig. 8(b), as a proxy for the Stokes–Einstein (SE) relation (since the collective relaxation time is well-known to behave similarly to the system viscosity), we can assess the amount of deviation with respect to SE, that is usually considered a feature of heterogeneous dynamics occurring close to the glass transition. We find that $D\tau_\alpha$ deviates from a constant more steeply for the attractive cases, in agreement with results on colloidal glasses.[81] On the other hand, the data for the purely repulsive case, where only the Hertzian is present, display a much reduced deviation from Stokes–Einstein, reminiscent of previous work on soft and ultra-soft potentials, such as star polymers.[82]

To have an operational definition of the glass transition, since we cannot rely on the power-law fits, we consider the system to be "arrested" within the simulation timescale when $D \lesssim 10^{-4}$ (in simulation units). Similarly, we attribute that the onset of the nonergodicity corresponds with a relaxation time $\tau_\alpha \gtrsim 10^3$. With these definitions, we can draw a tentative line of dynamic arrest of our copolymer microgels as a function of ϕ in a summarizing state diagram, reported in Fig. 8(c), which confirms the fact that by increasing T, the system arrests at a lower packing fraction. In the figure, we also show the values of the VPTT for pure PNIPAM microgels and for the present ones as a reference and notice that the macroscopic phase separation region seems to occur only above the VPT temperature. Simulations also suggest that the arrest line meets the tentative binodal on its right-hand side, leaving a liquid pocket at high ϕ and T in between the region of phase separated states and dynamically arrested states.

4 Conclusions

In this work we reported an investigation, combining SANS experiments and numerical simulations, of the temperature and concentration dependent interactions and state diagram of copolymer microgels made of PNIPAM and PEGMA. SANS data measured for moderately concentrated dispersions below and above the VPTT were accurately modeled at different packing fractions by calculating static structure factors using the effective interaction potentials obtained from simulations. At T = 20 °C the system is well described by a Hertzian model with the interaction being repulsive and rather soft, as indicated also by the fact that use of the star polymer potential also provides a good description of the experimental structure factors. Increasing temperature, the interaction as expected becomes more and more attractive. Already at T = 30 °C, well below the VPTT occurring for PNIPAM–PEGMA microgels around VPTT $\sim$ 37 °C, we find evidence of a weak attraction $\sim 1k_BT$ at its minimum. This indicates that the fraction of PEGMA chains that resides in the interior of the microgel hinders a complete collapse of the network and enhance the exterior hydrophobic interactions rather than screening them. Further increase of T above the VPTT induces the occurrence of phase separation already at quite low packing fractions ($\sim$0.15–0.20). It will be interesting in the future to compare these results with detailed studies of PNIPAM homopolymer microgels.

The SANS experiments also allow us to get useful insights on the modification of the interior structure of the particle as a function of microgel concentration. In particular, we find the interesting result that below the VPTT a significant reduction of the particle core radius and polymer blob scattering is observed well before particle overlap with increasing concentration. On the basis of previous studies,[65] we interpret this finding as associated with a concentration dependent osmotic unbalance arising from the presence of residual charges on the surface of the particles due to the use of an ionic initiator in the synthesis. In comparison with previous investigations, the reduction of the particle size appears to be more pronounced, which could be attributed to the larger softness of the poorly cross-linked particles used in this study, that is associated with the star-like particle architecture. In agreement with this interpretation, the reduction becomes almost negligible in the deswollen, compact state above the VPTT.

Using the effective interaction potential validated by comparison with SANS experiments, we additionally performed simulations to explore the state diagram of the system in the region of large packing fractions at the three studied temperatures. We find that, well below the VPTT (T = 20 °C), an arrested state, dominated by the Hertzian repulsion, is formed at large packing fractions $\phi_g^l \gtrsim 0.8$, with the large value of ϕ_g^l compared to hard-sphere like particles arising from the pronounced particle softness and polydispersity. This state is characterized by a structure factor that becomes non-monotonic in its first peak and goes below 1 at high concetrations. Instead, at intermediate temperatures (T = 30 °C) an arrested state is already formed at considerably smaller packing fractions, $\phi_g^h \gtrsim 0.63$, due to the presence of the weak attraction induced by the increasing hydrophobic character of the PNIPAM monomers and the increased compactness of the particles. Finally, above the VPTT for PNIPAM–PEGMA copolymer microgels (T = 40 °C), we find evidence of phase separation at low packing fraction, $\phi_g^h \sim 0.15$, whereas an arrested state emerges at $\phi_g^h \gtrsim 0.56$. An important difference in the numerical model with respect to homopolymer PNIPAM microgels is found in the α-values that are found to reproduce the experimental behavior. While for PNIPAM microgels the VPTT, occurring at $\sim$32 °C, corresponds to roughly $\alpha \sim 0.65$,[8,50,51] here we find that a smaller value of $\alpha \sim 0.58$ describes the data above the VPTT. We recall that α quantifies the strength of solvophobic attraction between NIPAM monomers only and, thus, it is possible that for copolymer microgels where also additional interactions between PNIPAM and PEGMA are at play, the scale of such effective temperature changes. It will be important to further test this hypothesis for different kinds of copolymer microgels in the future. Finally, it will also be interesting to investigate the high concentration regime and the approach to the arrest in future experiments in order to validate the numerical findings. In particular, it would be intriguing to verify whether there exists a pocket of liquid states at high ϕ and T, as well as the anomalous behavior of $S(Q)$ and to gain more complete information about the tunable interactions of copolymer microgels below and above the VPTT.

Conflicts of interest

There are no conflicts to declare.

Acknowledgements

We thank Fabrizio Camerin for valuable discussions and Gavino Bassu for assistance with the SEM measurements. R. R.-B., M. L.-P. and M. L. acknowledge support from the project ''A1-S-9098'' funded by Conacyt within the call ''Convocatoria de Investigación Básica 2017–2018'' and from ''Consorzio per lo Sviluppo dei Sistemi a Grande Interfase'' (CSGI). R. R.-B. and E. Z. acknowledge funding from H2020 Marie Curie Actions of the European Commission (ITN SUPER-COL, Grant Agreement 860914). We acknowledge the support of the National Institute of Standards and Technology, U.S. Department of Commerce, in providing the neutron research facilities used in this work and Y. Liu for assistance in using beamline NG7.

Notes and references

1 M. Stieger, W. Richtering, J. S. Pedersen and P. Lindner, *J. Chem. Phys.*, 2004, **120**, 6197–6206.

2 V. Nigro, R. Angelini, M. Bertoldo, V. Castelvetro, G. Ruocco and B. Ruzicka, *J. Non-Cryst. Solids*, 2015, **407**, 361–366.

3 T. Colla, P. S. Mohanty, S. Nöjd, E. Bialik, A. Riede, P. Schurtenberger and C. N. Likos, *ACS Nano*, 2018, **12**, 4321–4337.

4 B. Sierra-Martin, J. J. Lietor-Santos, A. Fernandez-Barbero, T. T. Nguyen and A. Fernandez-Nieves, *Microgel Suspensions: Fundamentals and Applications*, 2011, pp. 71–116.

5 F. Scheffold, *Nat. Commun.*, 2020, **11**, 1–13.

6 L. Rovigatti, N. Gnan, A. Ninarello and E. Zaccarelli, *Macromolecules*, 2019, **52**, 4895–4906.
7 K. Kubota, S. Fujishige and I. Ando, *J. Phys. Chem.*, 1990, **94**, 5154–5158.
8 A. Ninarello, J. J. Crassous, D. Paloli, F. Camerin, N. Gnan, L. Rovigatti, P. Schurtenberger and E. Zaccarelli, *Macromolecules*, 2019, **52**, 7584–7592.
9 L. Tavagnacco, E. Zaccarelli and E. Chiessi, *Phys. Chem. Chem. Phys.*, 2018, **20**, 9997–10010.
10 J. Wu, G. Huang and Z. Hu, *Macromolecules*, 2003, **36**, 440–448.
11 I. Bischofberger and V. Trappe, *Sci. Rep.*, 2015, **5**, 1–10.
12 Y. Bae, W.-D. Jang, N. Nishiyama, S. Fukushima and K. Kataoka, *Mol. BioSys.*, 2005, **1**, 242–250.
13 Y. Guan and Y. Zhang, *Soft Matter*, 2011, **7**, 6375–6384.
14 D. R. Griffin, W. M. Weaver, P. O. Scumpia, D. Di Carlo and T. Segura, *Nat. Mater.*, 2015, **14**, 737–744.
15 M. M. Ali, S. Su, C. D. Filipe, R. Pelton and Y. Li, *Chem. Commun.*, 2007, 4459–4461.
16 S. Schmidt, M. Zeiser, T. Hellweg, C. Duschl, A. Fery and H. Möhwald, *Adv. Funct. Mater.*, 2010, **20**, 3235–3243.
17 D. Gan and L. A. Lyon, *Macromolecules*, 2002, **35**, 9634–9639.
18 W. Leobandung, H. Ichikawa, Y. Fukumori and N. A. Peppas, *J. Appl. Polym. Sci.*, 2003, **87**, 1678–1684.
19 I. Berndt, J. S. Pedersen and W. Richtering, *J. Am. Chem. Soc.*, 2005, **127**, 9372–9373.
20 G. R. Hendrickson, M. H. Smith, A. B. South and L. A. Lyon, *Adv. Funct. Mater.*, 2010, **20**, 1697–1712.
21 M. Cors, O. Wrede, A.-C. Genix, D. Anselmetti, J. Oberdisse and T. Hellweg, *Langmuir*, 2017, **33**, 6804–6811.
22 L. Zha, Y. Zhang, W. Yang and S. Fu, *Adv. Mater.*, 2002, **14**, 1090–1092.
23 G. Zhou, A. Elaissari, T. Delair and C. Pichot, *Colloid Polym. Sci.*, 1998, **276**, 1131–1139.
24 N. Welsch, Y. Lu, J. Dzubiella and M. Ballauff, *Polymer*, 2013, **54**, 2835–2849.
25 X. Xia and Z. Hu, *Langmuir*, 2004, **20**, 2094–2098.
26 V. Nigro, R. Angelini, M. Bertoldo, E. Buratti, S. Franco and B. Ruzicka, *Polymers*, 2021, **13**, 1353.
27 V. Y. Rudyak, E. Y. Kozhunova and A. V. Chertovich, *Soft Matter*, 2020, **16**, 4858–4865.
28 E. Y. Kozhunova, V. Y. Rudyak, X. Li, M. Shibayama, G. S. Peters, O. V. Vyshivannaya, I. R. Nasimova and A. V. Chertovich, *J. Colloid Interface Sci.*, 2021, **597**, 297–305.
29 M. Keerl, V. Smirnovas, R. Winter and W. Richtering, *Macromolecules*, 2008, **41**, 6830–6836.
30 M. Keerl, J. S. Pedersen and W. Richtering, *J. Am. Chem. Soc.*, 2009, **131**, 3093–3097.
31 J. Es Sayed, C. Lorthioir, P. Perrin and N. Sanson, *Soft Matter*, 2019, **15**, 963–972.
32 R. Rivas-Barbosa, J. Ruiz-Franco, M. A. Lara-Peña, J. Cardellini, A. Licea-Claverie, F. Camerin, E. Zaccarelli and M. Laurati, *Macromolecules*, 2022, **55**, 1834–1843.
33 A. Serrano-Medina, J. Cornejo-Bravo and A. Licea-Claveríe, *J. Colloid Interface Sci.*, 2012, **369**, 82–90.
34 G. Del Monte, F. Camerin, A. Ninarello, N. Gnan, L. Rovigatti and E. Zaccarelli, *J. Phys.: Condens. Matter*, 2020, **33**, 084001.
35 C. Graf and A. van Blaaderen, *Langmuir*, 2002, **18**, 524–534.
36 C. M. Soukoulis and M. Wegener, *Nat. Photonics*, 2011, **5**, 523–530.
37 K. Uhlig, T. Wegener, J. He, M. Zeiser, J. Bookhold, I. Dewald, N. Godino, M. Jaeger, T. Hellweg and A. Fery, *et al.*, *Biomacromolecules*, 2016, **17**, 1110–1116.
38 M. Zhang, X. Li, Y. Gong, N. Zhao and X. Zhang, *Biomaterials*, 2002, **23**, 2641–2648.
39 K. Bjugstad, K. Lampe, D. Kern and M. Mahoney, *J. Biomed. Mater. Res., Part A*, 2010, **95**, 79–91.
40 L. Luo Zheng, V. Vanchinathan, R. Dalal, J. Noolandi, D. J. Waters, L. Hartmann, J. R. Cochran, C. W. Frank, C. Q. Yu and C. N. Ta, *J. Biomed. Mater. Res., Part A*, 2015, **103**, 3157–3165.
41 L. Hartmann, K. Watanabe, L. L. Zheng, C.-Y. Kim, S. E. Beck, P. Huie, J. Noolandi, J. R. Cochran, C. N. Ta and C. W. Frank, *J. Biomed. Mater. Res., Part B*, 2011, **98**, 8–17.
42 M. Lara-Peña, A. Licea-Claverie, I. Zapata-González and M. Laurati, *J. Colloid Interface Sci.*, 2021, **587**, 437–445.
43 J. S. Hyatt, C. Do, X. Hu, H. S. Choi, J. W. Kim, L. A. Lyon and A. Fernandez-Nieves, *Phys. Rev. E: Stat., Nonlinear, Soft Matter Phys.*, 2015, **92**, 030302.
44 X. Di, X. Peng and G. B. McKenna, *J. Chem. Phys.*, 2014, **140**, 054903.
45 C. Agbugba, B. Hendriksen, B. Chowdhry and M. Snowden, *Colloids Surf., A*, 1998, **137**, 155–164.
46 R. Pelton, *Adv. Colloid Interface Sci.*, 2000, **85**, 1–33.
47 K. Kremer and G. S. Grest, *J. Chem. Phys.*, 1990, **92**, 5057–5086.
48 T. Soddemann, B. Dünweg and K. Kremer, *Eur. Phys. J. E: Soft Matter Biol. Phys.*, 2001, **6**, 409–419.
49 F. Lo Verso, J. A. Pomposo, J. Colmenero and A. J. Moreno, *Soft Matter*, 2015, **11**, 1369–1375.
50 N. Gnan, L. Rovigatti, M. Bergman and E. Zaccarelli, *Macromolecules*, 2017, **50**, 8777–8786.
51 A. J. Moreno and F. L. Verso, *Soft Matter*, 2018, **14**, 7083–7096.
52 R. Chudoba, J. Heyda and J. Dzubiella, *J. Chem. Theory Comput.*, 2017, **13**, 6317–6327.
53 C. N. Likos, *Phys. Rep.*, 2001, **348**, 267–439.
54 R. Blaak, B. Capone, C. N. Likos and L. Rovigatti, *Forschungszentrum Jülich*, 2015, 209–258.
55 D. Paloli, P. S. Mohanty, J. J. Crassous, E. Zaccarelli and P. Schurtenberger, *Soft Matter*, 2013, **9**, 3000–3004.
56 A. G. Mailer, P. S. Clegg and P. N. Pusey, *J. Phys.: Condens. Matter*, 2015, **27**, 145102.
57 D. A. Sivak, J. D. Chodera and G. E. Crooks, *J. Phys. Chem. B*, 2014, **118**, 6466–6474.
58 J. Ruiz-Franco, L. Rovigatti and E. Zaccarelli, *Eur. Phys. J. E: Soft Matter Biol. Phys.*, 2018, **41**, 1–13.
59 J. S. Higgins and H. C. Benoit, *Polymers and Neutron Scattering*, Clarendon Press, 1st edn, 1997.
60 W. D. Dozier, J. S. Huang and L. J. Fetters, *Macromolecules*, 1991, **24**, 2810–2814.
61 J. Clara-Rahola, A. Fernandez-Nieves, B. Sierra-Martin, A. B. South, L. A. Lyon, J. Kohlbrecher and A. Fernandez Barbero, *J. Chem. Phys.*, 2012, **136**, 214903.

62 C. Likos, H. Löwen, M. Watzlawek, B. Abbas, O. Jucknischke, J. Allgaier and D. Richter, *Phys. Rev. Lett.*, 1998, **80**, 4450.

63 M. Doucet, J. H. Cho, G. Alina, J. Bakker, W. Bouwman, P. Butler, K. Campbell, M. Gonzales, R. Heenan, A. Jackson, P. Juhas, S. King, P. Kienzle, J. Krzywon, A. Markvardsen, T. Nielsen, L. O'Driscoll, W. Potrzebowski, R. F. Leal, T. Richter, P. Rozycko, T. Snow and A. Washington, *SasView version 4.1.2*, 2017.

64 S. G. Hatzikiriakos, *Soft Matter*, 2015, **11**, 7851–7856.

65 A. Scotti, U. Gasser, E. S. Herman, M. Pelaez-Fernandez, J. Han, A. Menzel, L. A. Lyon and A. Fernández-Nieves, *Proc. Natl. Acad. Sci. U. S. A.*, 2016, **113**, 5576–5581.

66 U. Gasser, A. Scotti and A. Fernandez-Nieves, *Phys. Rev. E*, 2019, **99**, 042602.

67 K. Kratz, A. Lapp, W. Eimer and T. Hellweg, *Colloids Surf., A*, 2002, **197**, 55–67.

68 M. Wolfe and C. Scopazzi, *J. Colloid Interface Sci.*, 1989, **133**, 265–277.

69 A. Jusufi, C. N. Likos and H. Löwen, *Phys. Rev. Lett.*, 2001, **88**, 018301.

70 I. Romero-Sanchez, I. Pihlajamaa, N. Adžic, L. E. Castellano, E. Stiakakis, C. N. Likos and M. Laurati, *ACS Nano*, 2022, **16**, 2133–2146.

71 I. C. Romero-Sanchez, L. E. Castellano and M. Laurati, *Macromolecules*, 2022, **55**, 4459–4468.

72 J. E. Houston, L. Fruhner, A. de la Cotte, J. R. González, A. V. Petrunin, U. Gasser, R. Schweins, J. Allgaier, W. Richtering, A. Fernandez-Nieves and A. Scotti, *Sci. Adv.*, 2022, **8**, eabn6129.

73 M. Daoud and J. P. Cotton, *J. Phys.*, 1982, **43**, 531–538.

74 G. Del Monte, D. Truzzolillo, F. Camerin, A. Ninarello, E. Chauveau, L. Tavagnacco, N. Gnan, L. Rovigatti, S. Sennato and E. Zaccarelli, *Proc. Natl. Acad. Sci. U. S. A.*, 2021, **118**, e2109560118.

75 P. Pusey, *Liquids, freezing and the glass transition*, North-Holland, Amsterdam, 1991.

76 L. Berthier, A. J. Moreno and G. Szamel, *Phys. Rev. E: Stat., Nonlinear, Soft Matter Phys.*, 2010, **82**, 060501.

77 F. Camerin, N. Gnan, J. Ruiz-Franco, A. Ninarello, L. Rovigatti and E. Zaccarelli, *Phys. Rev. X*, 2020, **10**, 031012.

78 M. J. Bergman, N. Gnan, M. Obiols-Rabasa, J.-M. Meijer, L. Rovigatti, E. Zaccarelli and P. Schurtenberger, *Nat. Commun.*, 2018, **9**, 1–11.

79 F. Roosen-Runge, A. Gulotta, S. Bucciarelli, L. Casal-Dujat, T. Garting, N. Skar-Gislinge, M. Obiols-Rabasa, B. Farago, E. Zaccarelli and P. Schurtenberger, *et al.*, *Biophys. J.*, 2020, **119**, 2483–2496.

80 N. Skar-Gislinge, F. Camerin, A. Stradner, E. Zaccarelli and P. Schurtenberger, *Mol. Pharmaceutics*, 2023, **20**, 2738–2753.

81 A. M. Puertas, C. De Michele, F. Sciortino, P. Tartaglia and E. Zaccarelli, *J. Chem. Phys.*, 2007, **127**, 144906.

82 S. Gupta, J. Stellbrink, E. Zaccarelli, C. N. Likos, M. Camargo, P. Holmqvist, J. Allgaier, L. Willner and D. Richter, *Phys. Rev. Lett.*, 2015, **115**, 128302.